

This manuscript is a preprint and has not been reviewed.

It is under review at *Journal of Climate*.

Copyright in this work may be transferred without further notice.

1

2 **Decomposing the Drivers of Polar Amplification with a Single Column**

3 **Model**

4 Matthew Henry*

5 *College of Engineering, Mathematics and Physical Sciences, University of Exeter, Exeter, UK*

6 Timothy M. Merlis

7 *Department of Atmospheric and Oceanic Sciences, McGill University, Montreal, Quebec,*

8 *Canada*

9 Nicholas J. Lutsko

10 *Scripps Institution of Oceanography, University of California at San Diego, La Jolla, CA, USA*

11 Brian E.J. Rose

12 *Department of Atmospheric and Environmental Sciences, University at Albany (State University*

13 *of New York), USA*

14 *Corresponding author address: Matthew Henry, College of Engineering, Mathematics and Phys-
15 ical Sciences, Harrison Building, Streatham Campus, University of Exeter, North Park Road, Ex-
16 eter, UK, EX4 4QF.

17 E-mail: m.henry@exeter.ac.uk

ABSTRACT

18 The precise mechanisms driving Arctic amplification are still under de-
19 bate. Previous attribution methods compute the vertically-uniform temper-
20 ature change required to balance the top-of-atmosphere energy imbalance
21 caused by each forcing and feedback, with any departures from vertically-
22 uniform warming collected into the lapse-rate feedback. We propose an al-
23 ternative attribution method using a single column model that accounts for
24 the forcing-dependence of high latitude lapse-rate changes. We examine this
25 method in an idealized General Circulation Model (GCM), finding that, even
26 though the column-integrated carbon dioxide (CO₂) forcing and water vapor
27 feedback are stronger in the tropics, they contribute to polar-amplified sur-
28 face warming as they produce bottom-heavy warming in high latitudes. A
29 separation of atmospheric temperature changes into local and remote contrib-
30 utors shows that, in the absence of polar surface forcing (e.g., sea-ice retreat),
31 changes in energy transport are primarily responsible for the polar amplified
32 pattern of warming. The addition of surface forcing substantially increases
33 polar surface warming and reduces the contribution of atmospheric dry static
34 energy transport to the warming. This physically-based attribution method
35 can be applied to comprehensive GCMs to provide a clearer view of the mech-
36 anisms behind Arctic amplification.

37 **1. Introduction**

38 The Arctic amplification of surface temperature change is a robust feature of observations
39 (Stocker et al. 2013) and comprehensive climate model simulations (Pithan and Mauritsen 2014).
40 A number of mechanisms are thought to contribute to Arctic amplification, including the surface
41 albedo feedback, increased atmospheric energy transport convergence (Hwang and Frierson 2010),
42 and the temperature feedback (Pithan and Mauritsen 2014); however, the precise contribution of
43 each mechanism is still unclear. Clarifying how these different factors contribute to Arctic ampli-
44 fication is essential for reducing the uncertainty in the rate of Arctic warming through improved
45 process-level understanding.

46 The tropics differ from the high latitudes in that they are close to radiative-convective equilib-
47 rium: heating by convection is balanced by radiative cooling, and the vertical temperature profile
48 is mostly determined by surface temperature and humidity, hence the vertical structure of tem-
49 perature change in the tropics is largely insensitive to the perturbation type. The high latitudes,
50 on the other hand, are close to radiative-advective equilibrium: warming from horizontal atmo-
51 spheric heat transport is balanced by cooling from radiation. This means that different forcings
52 and feedbacks induce different lapse rate responses. For example, an increase in longwave op-
53 tical depth leads to bottom-heavy warming (Cronin and Jansen 2016; Henry and Merlis 2020),
54 whereas atmospheric energy transport is thought to primarily affect the midtroposphere at high
55 latitudes (Laliberté and Kushner 2013; Feldl et al. 2017). This implies that the ratio between sur-
56 face warming and top-of-atmosphere (TOA) net radiation changes at high latitudes is different for
57 each forcing and feedback. Surface temperature change attributions based on TOA budget anal-
58 yses (Pithan and Mauritsen 2014) compute the vertically-uniform temperature change required to
59 balance the top-of-atmosphere energy imbalance caused by each forcing and feedback, with any

60 departures from vertically-uniform warming collected into the lapse-rate feedback. In these at-
61 tributions, the lapse rate feedback functions as a residual that can not be clearly ascribed to any
62 particular physical process and can obscure the true drivers of Arctic amplification. Similarly,
63 moist energy balance models (e.g. Roe et al. 2015) assume a linear relationship between changes
64 in surface temperature change and changes in net TOA radiation, and hence do not account for
65 the different vertical structures of the high latitude temperature responses to CO₂ forcing and to
66 changes in atmospheric energy transport convergence. Feldl et al. (2020) decompose the high lati-
67 tude lapse rate feedback into an upper component driven mainly by poleward atmospheric energy
68 transport and a lower component driven by local sea-ice loss. They find an increased contribution
69 to Arctic amplification for the combined albedo and lower lapse rate feedback, while the combined
70 water vapor and upper lapse rate feedback contribute equally to tropical and Arctic warming.

71 The coupled atmosphere surface climate feedback response analysis method (CFRAM) is a ver-
72 tically resolved version of the previously mentioned TOA energy budget method (Lu and Cai
73 2009). The local radiative response to temperature is linearized to infer the magnitude of the tem-
74 perature change that balances any energy flux perturbation. Using CFRAM, Taylor et al. (2013)
75 found that an increase in CO₂ and water vapor leads to bottom-heavy warming at high latitudes
76 (their figure 2 and 3c) and convection leads to top-heavy warming at low latitudes (their figure 8c).

77 Process-oriented and mechanism-denial experiments are useful tools for studying the mecha-
78 nisms responsible for Arctic amplification. For example, the analysis from Stuecker et al. (2018)
79 suggests that local forcings and feedbacks dominate the polar-amplified pattern of surface temper-
80 ature change in a comprehensive GCM in which CO₂ concentrations are increased in restricted
81 latitudinal bands. They find that restricting the CO₂ forcing to high latitudes produces a polar-
82 amplified warming structure, whereas restricting the CO₂ forcing to the tropics or mid-latitudes
83 leads to a more latitudinally-uniform temperature change. However, this result may be model-

84 dependent: Shaw and Tan (2018) show that restricting the CO₂ forcing to the tropics also leads to
85 a polar-amplified surface temperature change in two different comprehensive climate models with
86 aquaplanet lower boundary conditions. Stuecker et al. (2018) also show that the vertical structure
87 of high latitude warming depends on where the CO₂ forcing is applied: a midlatitude CO₂ forcing
88 leads to a more vertically uniform warming due to the effect of advection (Laliberté and Kushner
89 2013), whereas a high latitude CO₂ forcing leads to a surface-enhanced warming structure. Screen
90 et al. (2012) attribute near-surface warming to local forcings and feedbacks and warming aloft to
91 atmospheric energy transport increases by prescribing local and remote sea surface temperature
92 (SST) and sea ice concentration (SIC) changes in two comprehensive atmospheric GCMs. But,
93 prescribing SST where the model would otherwise warm (or cool) the surface is akin to imposing
94 a surface heat sink (or source), hence the results are not easily interpretable.

95 While these comprehensive GCM studies provide important insights into the mechanisms of
96 Arctic amplification, a hierarchy of models is required for a complete understanding of the drivers
97 of Arctic amplification in climate models and observations. Previous work using single column
98 model representations of the high latitude atmosphere suggested that the high latitude temperature
99 response is sensitive to the forcing type (Abbot and Tziperman 2008; Payne et al. 2015). Cronin
100 and Jansen (2016) have developed a 1-dimensional model of an atmosphere in radiative-advective
101 equilibrium for the high latitudes, which led to the important insight that high latitude lapse rate
102 changes are forcing-dependent. The present work seeks to bridge the gap between their simple
103 radiative-advective column model and complex climate model simulations in order to advance our
104 understanding of the drivers of Arctic amplification.

105 Using an idealized moist atmospheric GCM with aquaplanet surface boundary conditions, no
106 clouds, and no sea ice (hence no surface albedo feedback), we qualitatively reproduce the pattern
107 of surface temperature change from comprehensive GCMs in response to quadrupled CO₂. To

108 simulate the effect of melting sea ice, we impose a polar surface heat source, ranging from 0 to 24
109 W m^{-2} . Then, we use a single column model (SCM) to emulate the tropics and high latitudes of the
110 idealized GCM. This allows us to calculate the response to each individual forcing and feedback
111 and thus decompose the drivers of tropical and polar temperature change. This physically-based
112 attribution method does not attribute any warming to the lapse rate feedback. Instead, each forcing
113 and feedback's surface temperature change attribution already accounts for their impact on the
114 vertical structure of temperature change. The SCM attribution method builds on CFRAM by using
115 a convection scheme, which allows the SCM to be run as an "offline" version of the original GCM,
116 with the exception of horizontal energy transports and changes in heating due to condensation,
117 which still have to be taken from the GCM (or observations). The SCM can then be used to
118 perform feedback-locking experiments, hence is a valuable tool for untangling the drivers of polar
119 amplification. The idealized GCM acts as a test-case for the attribution method, which could
120 potentially be used to untangle the contributions of the various mechanisms of polar amplification
121 in comprehensive models.

122 **2. Idealized atmospheric GCM**

123 We use an idealized moist atmospheric GCM based on the Geophysical Fluid Dynamics Lab-
124 oratory (GFDL) spectral dynamical core and the comprehensive radiation scheme of the GFDL
125 AM2 GCM, with no sea ice or clouds. This is similar to the setup in Merlis et al. (2013) and to
126 the Model of an Idealized Moist Atmosphere (MiMA, Jucker and Gerber (2017)). These GCMs
127 follow the moist idealized GCM described in Frierson et al. (2006), but use comprehensive clear-
128 sky radiation instead of grey radiation. In the MiMA setup, the surface albedo is globally uniform
129 and increased to compensate for the cooling effect of clouds. In Merlis et al. (2013), an idealized
130 cloud distribution is prescribed for the radiative transfer calculation. Here, there are no clouds and

131 we set the surface albedo to a hemispherically symmetric analytic distribution similar to Earth's
132 northern hemisphere TOA albedo, as estimated from the Cloud and the Earth's Radiant Energy
133 System data (Loeb et al. (2018), see supplemental figure S1), in order to produce an Earth-like
134 meridional surface temperature gradient. The model uses the comprehensive radiation scheme de-
135 scribed in Anderson et al. (2004), with annual-mean solar insolation and a solar constant equal to
136 1365 W m^{-2} .

137 The surface boundary condition is a slab mixed layer ocean aquaplanet with no representation of
138 ocean heat transport and the heat capacity of 1m of water. We use annual-mean insolation and the
139 small mixed layer depth allows the model to equilibrate quickly without meaningfully affecting
140 the model's climate, as we only consider time-independent boundary conditions and forcing. The
141 GCM was run at T42 spectral truncation, for a nominal horizontal resolution of $2.8^\circ \times 2.8^\circ$, and
142 with 30 vertical levels. The skin temperature is interactively computed using the surface radiative
143 and turbulent fluxes, which are determined by bulk aerodynamic formulae. A k-profile scheme
144 with a dynamically determined boundary layer height is used to parameterize the boundary layer
145 turbulence. The GCM uses a simplified Betts-Miller convection scheme (Frierson 2007), and
146 large scale condensation is parameterized such that the relative humidity does not exceed one and
147 condensed water is assumed to immediately return to the surface. As there is no representation of
148 sea ice, there is no surface albedo feedback. To mimic the presence of the surface albedo feedback,
149 we run perturbation experiments with an added polar surface heat source. All simulations are run
150 for 20 years with time averages over the last 10 years shown, when all climate states have reached
151 a statistical steady state.

152 We perform four simulations: a control run in which the atmospheric CO_2 concentration is set
153 to 300 ppm, a run with quadrupled (1200 ppm) CO_2 concentration, and two runs with quadrupled
154 CO_2 concentrations and constant surface heat sources Q_s of 12 W m^{-2} and 24 W m^{-2} poleward

155 of 80° in both hemispheres. The heat sources simulate surface heating through the surface albedo
156 feedback or a large increase in oceanic energy transport convergence. Given that the polar surface
157 temperature change under $4xCO_2$ is approximately 8K, a 12 (24) $W m^{-2}$ surface heat source is
158 equivalent to a 1.5 (3) $W m^{-2} K^{-1}$ local feedback. This can be compared to the locally defined
159 surface albedo feedback from the models participating in the fifth coupled model intercompar-
160 ison project (CMIP5) which is approximately 1 $W m^{-2} K^{-1}$ in the Arctic and 2 $W m^{-2} K^{-1}$ in
161 the Southern Ocean (Feldl and Bordoni 2016, their figure 1). We note that the polar surface heat
162 source is not comparable to the annual-mean surface heat flux anomaly from comprehensive mod-
163 els which includes changes in the other terms of the surface energy budget.

164 Figure 1a shows the zonal-mean surface skin temperature differences between the control and
165 three perturbation simulations, in addition to the zonal-mean surface skin temperature responses
166 of abrupt $4xCO_2$ experiments with models participating in the sixth Coupled Model Intercompar-
167 ison Project (CMIP6) (Eyring et al. 2016), averaged over 50 years after 100 years of integration.
168 Figure 1b shows the surface temperature changes normalized by their global mean. The patterns
169 of surface temperature change from the idealized model experiments (black) approximately span
170 the CMIP6 model responses (grey). The amount of Arctic amplification is smaller in the ideal-
171 ized GCM's $4xCO_2$ experiment due to the lack of local positive feedbacks such as sea ice and
172 cloud feedbacks. However, adding a polar surface heat source brings the idealized GCM closer
173 to CMIP6 in the Arctic, which have high latitude warming of 2 to 4 times the global-mean sur-
174 face temperature change. Note that the CMIP6 temperature changes are not fully equilibrated,
175 and, at equilibrium, the Antarctic is also expected to have amplified warming, but this warming
176 is transiently delayed by upwelling in the Southern Ocean (Manabe et al. 1991; Rugenstein et al.
177 2019).

178 3. Single column model

179 To emulate the tropical and high-latitude atmosphere of the idealized GCM, we use the single
 180 column model (SCM) from the ClimLab python package for process-oriented climate modeling
 181 (Rose 2018). The atmospheric and surface temperature tendency budgets are given by:

$$\frac{\partial T_{atm}(p)}{\partial t} = \left. \frac{\partial T_{atm}(p)}{\partial t} \right|_{rad} + \left. \frac{\partial T_{atm}(p)}{\partial t} \right|_{conv} + \left. \frac{\partial T_{atm}(p)}{\partial t} \right|_{adv} + \left. \frac{\partial T_{atm}(p)}{\partial t} \right|_{cond} + \left. \frac{\partial T_{atm}(p)}{\partial t} \right|_{diff}, \quad (1)$$

$$\frac{\partial T_s}{\partial t} = \left. \frac{\partial T_s}{\partial t} \right|_{rad} + \left. \frac{\partial T_s}{\partial t} \right|_{conv} + Q_S/C_O + Q_{bias}/C_O, \quad (2)$$

182 where t is time and p is pressure (with 30 pressure levels), and C_O is the heat capacity of a unit
 183 area of water with a depth of 1 meter. The subscripts ‘rad’, ‘conv’, ‘adv’, ‘cond’, and ‘diff’ refer to
 184 radiative, convective, advective, condensation, and diffusive temperature tendencies, respectively.
 185 Q_S is the imposed surface heat source term ($0,12,24 \text{ W m}^{-2}$) and Q_{bias} is a bias term described
 186 below. The radiative and convective sensible heat flux, and latent heat flux temperature tendencies
 187 are computed interactively. The Rapid Radiative Transfer Model for GCMs (RRTMG) (Mlawer
 188 et al. 1997) radiation scheme is used for the computation of shortwave and longwave radiative
 189 temperature tendencies. The surface albedo and control insolation are set to idealized GCM values
 190 in the tropics (10°S to 10°N) and poleward of 80° . Convection is implemented as an adjustment of
 191 the temperature profile to the moist adiabat, whereas the idealized GCM uses a simplified Betts-
 192 Miller convection scheme (Frierson 2007). Note that at high latitudes, horizontal atmospheric
 193 energy transport induces a temperature structure stable to convection, hence convection has no
 194 effect.

195 Values from the idealized GCM experiments averaged in the tropics (10°S to 10°N) and pole-
 196 ward of 80°N are used to prescribe the specific humidity profile, which affects the radiation. In

197 addition, the time-mean advection and condensation temperature tendency profiles from the ide-
198 alized GCM simulations are added as external temperature tendency terms to simulate the dry
199 and moist components of atmospheric energy transport convergence respectively, and the diffu-
200 sive temperature tendency term is prescribed from the idealized GCM boundary layer scheme (see
201 supplementary figure S2 for the temperature tendency profiles). The advective temperature ten-
202 dency term is calculated in the GCM as the difference in temperature tendency before and after
203 running the dynamics module, hence it contains the horizontal and vertical advection temperature
204 tendencies and includes the effect of transient eddies. The SCM has no surface sensible and latent
205 heat fluxes, but, unlike the GCM, the surface energy budget has a convection term (equation 2),
206 as the SCM convection scheme applies the same critical lapse rate between the ground and the
207 first model level as it does between model levels (Manabe and Strickler 1964). Moreover, despite
208 having the same TOA insolation and surface albedo as the GCM, there is a difference in absorbed
209 shortwave radiation at the surface, which may be due to the difference in the amount of absorbed
210 shortwave radiation in the atmosphere by the two different radiation schemes. Hence, a bias term
211 (Q_{bias}) is added to account for the difference between the GCM's surface turbulent (sensible and
212 latent) heat fluxes and the SCM's surface convection term, and the bias in net surface shortwave
213 radiation: $Q_{bias} = (\text{GCM surface turbulent heat flux} - \text{SCM surface convective heat flux}) + (\text{GCM}$
214 $\text{absorbed shortwave at the surface} - \text{SCM absorbed shortwave at the surface})$. When we add a
215 surface heat source (Q_S) at high latitudes in the idealized GCM, the surface turbulent heat fluxes
216 are smaller, hence Q_{bias} is smaller. The values of Q_{bias} are tabulated in supplementary table S1.

217 The climatological temperature profiles of the idealized GCM and SCM are similar (figure 2).
218 Similarities between the temperature profiles simulated by the idealized GCM and by the SCM
219 still hold when the latitudinal bounds of the tropics are set to 20°S-20°N and the high latitudes to
220 60° (see supplementary figure S3).

221 **4. Attribution of idealized GCM tropical and polar lapse rate changes to forcings and feed-**
222 **backs.**

223 As discussed in the introduction, the forcing dependence of the high latitude lapse rate feedback
224 makes a TOA budget approach to attributing the polar surface warming to different forcings and
225 feedbacks ambiguous (see next section). The SCM allows us to attribute the idealized GCM's trop-
226 ical and polar lapse rate changes to the different forcings and feedbacks. The CO₂ concentration
227 is a single value in the SCM, whereas the water vapor and atmospheric energy transport profiles
228 (advection and condensation temperature tendencies in figure S2) are derived from the idealized
229 GCM experiments. We individually perturb CO₂, water vapor (in the radiative transfer scheme),
230 atmospheric energy transport (moist and dry components), and vertical diffusion in the tropics and
231 high latitudes to attribute the total warming to each of these individual components.

232 Figure 3 shows the decomposition of (a) tropical and (b,c,d) polar lapse rate changes of the
233 three idealized GCM perturbation experiments: 4xCO₂ (a,b), 4xCO₂ with $Q_s=12 \text{ W m}^{-2}$ (a,c) and
234 $Q_s=24 \text{ W m}^{-2}$ (a,d); Table 1 summarizes the surface temperature change attributions.

235 The tropical lapse rate changes for the three experiments are similar enough to be plotted in
236 the same figure 3a: the $Q_s = 12 \text{ W m}^{-2}$ and $Q_s = 24 \text{ W m}^{-2}$ experiment changes are shown in
237 dashed and dash-dotted respectively, and fall close to each other. The tropical lapse rate changes
238 are decomposed into the temperature change from the CO₂ forcing (red), changes due to verti-
239 cal diffusion (magenta), the water vapor feedback (blue), and energy transport (green). For each
240 GCM experiment, the SCM's response to applying all of the perturbations simultaneously (black)
241 is exactly the same as the sum of the responses to the individual perturbations and fits the ideal-
242 ized GCM's response well throughout the troposphere (grey), demonstrating the accuracy of the
243 attribution method. Differences in the stratosphere between the SCM and idealized GCM may

244 be due to the different radiation schemes or ozone distributions. Since convection is triggered in
245 the tropics, the temperature profiles are moist adiabatic and the vertical structure of tropospheric
246 temperature change ($\Delta T/\Delta T_S$) is approximately the same for all SCM experiments. The energy
247 transport is slightly reduced in the experiments with surface heat sources.

248 The polar lapse rate changes (b,c,d) are decomposed into the temperature changes from the CO₂
249 forcing (red), the change in vertical diffusion (magenta), the water vapor feedback (blue), the ‘lo-
250 cal’ water vapor feedback (blue dashed, see section 6), the energy transport (dry component in
251 orange and moist component in cyan), and the surface heat source (yellow). Again, for each GCM
252 experiment, the SCM’s response to applying all of the perturbations simultaneously (black) is ex-
253 actly the same as the sum of the responses to the individual perturbations, and fits the idealized
254 GCM’s response well throughout the troposphere (grey), though not as well as in the tropics. Dis-
255 crepancies between SCM (all) and the idealized GCM may be due to the lack of time fluctuations
256 in the SCM. The increase in longwave absorbers (CO₂ and water vapor) leads to bottom-heavy
257 warming, the dry component of energy transport leads to top-heavy warming, the moist compo-
258 nent of energy transport leads to mid-troposphere enhanced warming, and the surface heat source
259 leads to very bottom-heavy warming.

260 The polar surface temperature change is 4.8K and 8.6K higher in the $Q_s = 12\text{W m}^{-2}$ and $Q_s =$
261 24W m^{-2} cases, respectively, compared to the $Q_s = 0\text{W m}^{-2}$ case, which is caused mainly by 4.3K
262 and 7.2K warming, respectively, due to the surface heat source. Reductions in the dry component
263 of energy transport cause coolings of 1.8K and 3.8K respectively versus a 0.1K warming in the
264 simulation with $Q_s = 0\text{W m}^{-2}$. There are also slight increases in warming due to the water vapor
265 feedback (discussed in section 6), the moist component of the energy transport, and the diffusion
266 term compared to the 4xCO₂ experiment (Table 1). These results are consistent with Hwang et al.
267 (2011), who found that enhanced Arctic warming due to local feedbacks weakens the equator-

268 to-pole temperature gradient and reduces the dry component of the atmospheric energy transport,
 269 which outweighs the increase in the moist component of atmospheric energy transport that arises
 270 from the enhanced warming. Alexeev and Jackson (2013) also found that a strong surface albedo
 271 feedback reduces the polar atmospheric heat transport convergence. The lapse rate changes caused
 272 by changes in CO₂, water vapor, energy transport, and Q_S do not depend strongly on the inclusion
 273 of the vertical diffusion term in the SCM.

274 **5. Surface temperature change attribution method comparison**

275 The conventional surface temperature change attribution method (Pithan and Mauritsen 2014;
 276 Stuecker et al. 2018) computes the vertically-uniform temperature change required to balance the
 277 top-of-atmosphere energy imbalance caused by each forcing and feedback, with any departures
 278 from vertically-uniform warming collected into the lapse-rate feedback. The deviation from ver-
 279 tically uniform temperature change is then accounted for in the lapse rate feedback. One can
 280 decompose the surface temperature changes in the idealized GCM experiments as follows (similar
 281 to equation 3 in the Methods section of Stuecker et al. (2018)):

$$\Delta T_S(\phi) = \left(-\frac{1}{\lambda_P}\right) \{ \Delta T_S(\phi) [\lambda'_P(\phi) + \lambda_{LR}(\phi) + \lambda_{WV}(\phi)] + Q_S(\phi) + \mathcal{F}(\phi) + \Delta(\nabla \cdot \vec{F}(\phi)) \} \quad (3)$$

282 where ϕ is the latitude. The surface temperature change attributions are then given by the average
 283 of $\Delta T_S(\phi)$ over the tropics and Arctic. The Planck feedback is decomposed into its global-mean $\overline{\lambda_P}$
 284 and its deviation λ'_P , λ_{LR} is the lapse rate feedback, λ_{WV} is the water vapor feedback, Q_S is the sur-
 285 face forcing, and there would be an additional cloud feedback term if analyzing a comprehensive
 286 GCM.

287 To apply the conventional attribution method to the GCM simulations, we use aquaplanet ker-
288 nels derived from Isca (Vallis et al. 2018; Liu 2020) to calculate the feedbacks¹. The CO₂ forcing
289 \mathcal{F} is computed as the change in TOA net radiation between the control simulation and an ideal-
290 ized GCM simulation where sea surface temperatures (SST) are fixed to the control SST and CO₂
291 concentrations are quadrupled (Hansen et al. 2005). The change in atmospheric energy transport
292 convergence $\Delta(\nabla \cdot \vec{F})$ is computed as the change in net TOA radiation (minus the surface forcing)
293 between the control and perturbed simulations. This method of attributing surface temperature
294 changes to forcings and feedbacks then tells us how much surface temperature change is required
295 to balance the TOA energy imbalance caused by each forcing or feedback, assuming the atmo-
296 spheric temperature change is vertically uniform (except for the lapse rate feedback). There is no
297 explicit vertical diffusion in this TOA energy budget approach, in contrast to the vertically resolved
298 CFRAM. So, we do not include it in our comparison between SCM and TOA budget approach.

299 Figure 4 compares this TOA energy budget surface temperature change attribution method
300 (crosses) with the single column model based attribution method (filled circles) for the 4xCO₂
301 (a), 4xCO₂ with $Q_s = 12\text{W m}^{-2}$ (b) and $Q_s = 24\text{W m}^{-2}$ (c). The tropical (x-axis, 10°S to 10°N)
302 and polar (y-axis, 80°N to 90°N) attributions are plotted against each other. If a point falls above
303 (below) the one-to-one line, the forcing or feedback contributes to polar (tropical) amplification.
304 As in Pithan and Mauritsen (2014), the TOA attribution method suggests that the Planck feedback,
305 the lapse rate feedback, and increased horizontal energy transport are the primary drivers of polar
306 amplification. The lapse rate feedback contributes to more polar amplification in the surface heat
307 source experiments. The single column model attribution method, in contrast, has no temperature
308 feedback in its decomposition. Since the TOA energy budget method assumes that the temperature
309 response to a TOA energy imbalance is vertically uniform, it will attribute a larger (smaller) am-

¹Using aquaplanet kernels derived from the GFDL Atmospheric Model 2 leads to strong biases in the tropics due to its different mean state.

310 plitude change in surface temperature than the single column model if the response to the forcing
311 or feedback is top-heavy (bottom-heavy). In the tropics, all temperature changes are top-heavy
312 as they follow the moist adiabat, hence the SCM attributions are all closer to the y-axis than the
313 corresponding TOA method attributions. In the high latitudes, the SCM temperature changes from
314 increases in CO₂, water vapor, and surface heat source are bottom-heavy, hence they all contribute
315 a larger surface temperature change than is diagnosed from the TOA method. The energy trans-
316 port convergence change leads to top-heavy warming, hence the warming attributed to it by the
317 SCM method is smaller than the warming attributed by the TOA method, and even negative in the
318 surface heat source cases. The residual term (black), calculated as the difference between the sum
319 of each term and the actual surface temperature change, is small for all the simulations.

320 In summary, we underline two main points from this comparison of the single column model
321 and TOA-based surface temperature change attribution methods:

- 322 • The increase in longwave absorbers (CO₂ and water vapor) go from contributing to tropi-
323 cal amplification in the TOA attribution method to contributing to polar amplification in the
324 SCM attribution method. The forcing from CO₂ and the water vapor feedback are stronger
325 in the tropics than the high latitudes, but since the tropical SCM attribution includes the ef-
326 fect of convection, the warming maximum shifts into the upper-troposphere and there is less
327 surface warming. In the high latitudes however, an increase in longwave absorbers leads to
328 bottom-heavy warming (Taylor et al. 2013; Cronin and Jansen 2016; Henry and Merlis 2020).
329 Russotto and Biasutti (2020) analyze the response of atmospheric GCMs using a moist en-
330 ergy balance model, and similarly find that a tropically amplified CO₂ forcing and water vapor
331 feedback lead to a polar amplified temperature response.

332 • Since the increase in atmospheric energy transport convergence preferentially affects the mid-
 333 troposphere, it leads to less surface warming at high latitudes, and even to surface cooling in
 334 the surface heat source experiments. In contrast, the effect of the vertically integrated increase
 335 in atmospheric energy transport convergence would always be a surface warming in the TOA-
 336 budget based approach.

337 **6. Local and remote drivers of temperature change.**

338 The SCM attribution method can also be used to decompose polar amplification into its local and
 339 remote drivers. The CO₂ and surface heat source perturbations are local drivers, while the energy
 340 transport can be considered as a remote driver. The water vapor feedback includes both local and
 341 remote contributions. First, the change in specific humidity can be decomposed into a temperature-
 342 dependent change and a change due to relative humidity: $\Delta q = \Delta q|_{fixedRH} + \Delta RH \times q^*|_{clim}$
 343 where $q^*|_{clim}$ is the climatological saturation specific humidity. Since the relative humidity in
 344 the idealized GCM stays relatively constant (supplementary figure S4), we ignore the second
 345 term of this equation. Using fixed relative humidity (RH) SCM experiments, we can decom-
 346 pose the temperature-dependent changes in specific humidity into the ‘local’ changes in re-
 347 sponse to the temperature changes forced by increased CO₂ and the surface heat source, and
 348 the ‘remote’ changes in response to the temperature change forced by altered energy transports:

$$349 \Delta q \approx \Delta q|_{fixedRH} = \Delta q|_{fixedRH, \Delta CO_2, \Delta Q_s} + \Delta q|_{fixedRH, \Delta ET}.$$

350 This local versus remote decomposition of the water vapor concentration increase is not perfect,
 351 as it assumes the energy transport simply affects the humidity of the high latitudes by changing
 352 its temperature and activating the local water vapor feedback, whereas the general circulation can
 353 directly advect water vapor. The energy transport term also contains vertical advection, which can
 354 change as a result of local diabatic forcings (shown in magenta in supplementary figure S2). More-

355 over, GCM experiments where the forcing from a CO₂ increase is constrained to the high latitudes
356 show changes in energy transport, which would also affect the water vapor feedback (Stuecker
357 et al. 2018). Since energy transport is affected by both temperature and humidity gradients, it is
358 not clear that any perfect local / remote decomposition exists. Nevertheless, our definition of ‘lo-
359 cal’ recovers traditional SCM treatments of fixed relative humidity water vapor feedback (Manabe
360 and Wetherald 1967) in the limit of no changes in energy transport.

361 The fixed-RH SCM simulations have the same modules and parameters as the standard SCM
362 simulations, but instead of prescribing the idealized GCM’s specific humidity, they have fixed rel-
363 ative humidity and the specific humidity is free to evolve with temperature. The climatological
364 temperature of the fixed RH SCMs have a warm bias (supplementary figure S5) and the climato-
365 logical specific humidity is biased high (supplementary figures S6). We do two sets of fixed-RH
366 SCM experiments: the first (‘local’) experiment is forced with the increase in CO₂ concentration
367 (and surface heat source), and the second is forced with increased CO₂ concentration (and surface
368 heat source) and perturbed energy transport. The latter has less tropical warming and similar polar
369 warming compared to the idealized GCM (red lines in supplementary figure S7 for the 4xCO₂
370 experiment), and similar changes in specific humidity in the tropics and a higher increase in high
371 latitudes compared to the idealized GCM (red lines in supplementary figures S8 for the 4xCO₂
372 experiment). The ‘local’ increase in water vapor, $\Delta q|_{fixedRH, \Delta CO_2, \Delta Q_s}$, is taken to be the change in
373 water vapor from the first set of fixed-RH SCM experiments (blue lines in figure S8 for the 4xCO₂
374 experiment), and the ‘remote’ increase in water vapor, $\Delta q|_{fixedRH, \Delta ET}$, is taken to be the residual
375 between the total change in water vapor and the ‘local’ change in water vapor. We then force the
376 original SCM with the ‘local’ and ‘remote’ specific humidity changes to deduce the ‘q (local)’ and
377 ‘q (remote)’ temperature changes (shown in table 2). The ‘q (local)’ experiments are comparable

378 to the fixed RH experiments in Payne et al. (2015). The temperature changes from the high latitude
379 ‘q (local)’ experiments are shown in figure 3 (blue dashed).

380 Table 2 summarizes the result of this local / remote decomposition of surface temperature
381 change. In the three perturbation experiments, the warming from CO₂ alone is 1.9K in the tropics
382 and 3.3K at high latitudes, hence increasing CO₂ leads to polar amplification in the absence of any
383 feedbacks. The addition of the ‘local’ water vapor feedback increases the tropical surface warm-
384 ing to 12.2K and the polar surface warming to 4.4K in the 4xCO₂ experiment, and thus cancels
385 the polar amplification from CO₂ alone. Payne et al. (2015) also found a tropical amplification of
386 surface temperature change in their fixed-RH SCM simulations, though with somewhat different
387 magnitude. Finally, adding the atmospheric energy transport and its implied water vapor change
388 decreases the tropical surface warming to 3.5K, and increases the polar surface warming to 9.0K
389 in the 4xCO₂ experiment, thus leading to polar amplification. The polar surface heat source gen-
390 erally increases the amount of polar amplification despite the partial compensation by a reduction
391 in dry energy transport. For the 4xCO₂ experiment, approximately half of the polar warming is
392 due to local sources (4.0K out of 9K of total warming), but the polar amplified pattern of warming
393 is primarily caused by the increase in atmospheric energy transport which cools the tropics and
394 warms the high latitudes. The high latitude warming is then strongly enhanced by the increased
395 water vapor from remote sources. When a polar surface heat source is added, almost all of the
396 polar surface warming is due to local sources because of the surface heat source and the compen-
397 sating reduction in the dry component of energy transport: 11.2K and 16.6K from local sources
398 for a total warming of 13.8K and 17.6K for the $Q_s = 12\text{W m}^{-2}$ and $Q_s = 24\text{W m}^{-2}$ experiments,
399 respectively.

400 **7. Summary and discussion**

401 Unlike the tropics which are close to radiative-convective equilibrium, the high latitudes are in
402 radiative-advective equilibrium: different forcings and feedbacks induce different lapse rate re-
403 sponses. Previous surface temperature change attribution methods compute the vertically-uniform
404 temperature change required to balance the top-of-atmosphere energy imbalance caused by each
405 forcing and feedback, with any departures from vertically-uniform warming collected into the
406 lapse-rate feedback. In these attributions, the lapse rate feedback functions as a residual that can-
407 not be clearly ascribed to any particular physical process.

408 We introduce a surface temperature change attribution method based on a single column model,
409 which accounts for the vertically inhomogeneous temperature change contributions of each forcing
410 and feedback. We find that the warming from increased longwave absorbers (CO_2 and water vapor)
411 is bottom-heavy and accounts for most of the surface warming at high latitudes in the absence of
412 a surface heat source. By contrast, the warming from atmospheric heat transport preferentially
413 warms the mid and upper troposphere. The CFRAM method (Taylor et al. 2013) previously found
414 that the warming from increased CO_2 and water vapor leads to bottom-heavy warming at high
415 latitudes, and that convection leads to top-heavy warming at low latitudes. The single column
416 model has the additional feature of enabling an analysis of how different processes interact with
417 one another. Convection responds to radiative destabilization, which is particularly relevant in low
418 latitudes (Wang and Huang 2020) . And, when a polar surface heat source is added, there is a
419 reduction in the dry component of atmospheric energy transport which partially compensates for
420 the extra surface warming from the polar surface heat source.

421 Compared to the conventional surface temperature change attribution method, the increase in
422 longwave absorbers (CO_2 and water vapor) goes from contributing to tropical amplification to

423 polar amplification. In addition, the polar warming contribution from the increase in atmospheric
424 energy transport convergence is reduced as it preferentially warms the mid and upper troposphere.
425 Moreover, when a polar surface heat source is added, the contributions of the surface heat source
426 and the concomitant reduction in atmospheric energy transport are properly separated instead of
427 producing a larger lapse rate feedback contribution to polar amplification.

428 Finally, we separated the drivers of atmospheric temperature change into local and remote con-
429 tributors and found that, in the absence of a polar surface heat source, the change in energy trans-
430 port and the “remote” water vapor changes were primarily responsible for the polar amplified
431 pattern of warming. The addition of a polar surface heat source increases the contribution of local
432 drivers to polar warming at the expense of remote drivers, as the dry energy transport is reduced.

433 It is important to note that clouds and sea ice were ignored in this analysis (aside from the surface
434 heat source that mimics the effects of shortwave cloud feedbacks and sea ice), though they may
435 play an important role in explaining the pattern of surface temperature change in comprehensive
436 climate model simulations. Arctic amplification also has seasonality — it is strong in winter and
437 suppressed in summer — which has been suggested to result from the increased polar ocean heat
438 uptake in summer and ocean heat release in winter from the melting sea ice (Manabe and Stouffer
439 1980; Bintanja and Van der Linden 2013; Dai et al. 2019). Nevertheless, we believe that the single-
440 column model can be a stepping stone for connecting simple physical models with comprehensive
441 climate models: clouds and seasonality can be prescribed in the SCM, which would be a valuable
442 extension of the present work. This would allow us to understand the basic mechanisms driving
443 Arctic amplification.

444 *Acknowledgments.* The code and data needed to reproduce all figures, tables and supplementary
445 figures will be made available at https://github.com/matthewjhenry/HMLR19_SCM. Documenta-
446 tion for the python ClimLab package can be found at <https://climlab.readthedocs.io/>. The top-of-
447 atmosphere albedo data from the Cloud and the Earth’s Radiant Energy System (CERES) can be
448 found at <https://ceres.larc.nasa.gov/>. The CMIP6 data is available on the Earth System Grid Fed-
449 eration database. This work was supported by a Natural Sciences and Research Council (NSERC)
450 Discovery grant and Canada Research Chair, as well as a Compute Canada allocation. B.E.J.R
451 was supported by NSF grant AGS-1455071.

452 **References**

453 Abbot, D. S., and E. Tziperman, 2008: Sea ice, high-latitude convection, and equable climates.

454 *Geophysical Research Letters*, **35** (3).

455 Alexeev, V. A., and C. H. Jackson, 2013: Polar amplification: is atmospheric heat transport im-
456 portant? *Clim. Dyn.*, **41**, 533–547.

457 Anderson, J. L., and Coauthors, 2004: The new GFDL global atmosphere and land model AM2–
458 LM2: Evaluation with prescribed SST simulations. *Journal of Climate*, **17** (24), 4641–4673.

459 Bintanja, R., and E. Van der Linden, 2013: The changing seasonal climate in the arctic. *Scientific*
460 *Reports*, **3**, 1556.

461 Cronin, T. W., and M. F. Jansen, 2016: Analytic radiative-advective equilibrium as a model for
462 high-latitude climate. *Geophysical Research Letters*, **43** (1), 449–457.

463 Dai, A., D. Luo, M. Song, and J. Liu, 2019: Arctic amplification is caused by sea-ice loss under
464 increasing CO₂. *Nature communications*, **10** (1), 121.

465 Eyring, V., S. Bony, G. A. Meehl, C. A. Senior, B. Stevens, R. J. Stouffer, and K. E. Taylor, 2016:
466 Overview of the coupled model intercomparison project phase 6 (CMIP6) experimental design
467 and organization. *Geoscientific Model Development (Online)*, **9** (LLNL-JRNL-736881).

468 Feldl, N., B. T. Anderson, and S. Bordoni, 2017: Atmospheric eddies mediate lapse rate feedback
469 and arctic amplification. *Journal of Climate*, **30** (22), 9213–9224.

470 Feldl, N., and S. Bordoni, 2016: Characterizing the Hadley circulation response through regional
471 climate feedbacks. *J. Climate*, **29** (2), 613–622.

472 Feldl, N., S. Po-Chedley, H. K. Singh, S. Hay, and P. J. Kushner, 2020: Sea ice and atmospheric
473 circulation shape the high-latitude lapse rate feedback. *npj Climate and Atmospheric Science*,
474 **3** (1), 1–9.

475 Frierson, D. M., 2007: The dynamics of idealized convection schemes and their effect on the
476 zonally averaged tropical circulation. *J. Atmos. Sci.*, **64** (6), 1959–1976.

477 Frierson, D. M., I. M. Held, and P. Zurita-Gotor, 2006: A gray-radiation aquaplanet moist GCM.
478 part I: Static stability and eddy scale. *Journal of the Atmospheric Sciences*, **63** (10), 2548–2566.

479 Hansen, J., and Coauthors, 2005: Efficacy of climate forcings. *J. Geophys. Res.*, **110**, D18 104.

480 Henry, M., and T. M. Merlis, 2020: Forcing dependence of atmospheric lapse rate changes dom-
481 inates residual polar warming in solar radiation management climate scenarios. *Geophysical*
482 *Research Letters*, e2020GL087929.

483 Hwang, Y.-T., and D. M. Frierson, 2010: Increasing atmospheric poleward energy transport with
484 global warming. *Geophysical Research Letters*, **37** (24).

485 Hwang, Y.-T., D. M. Frierson, and J. E. Kay, 2011: Coupling between Arctic feedbacks and
486 changes in poleward energy transport. *Geophysical Research Letters*, **38** (17).

487 Jucker, M., and E. Gerber, 2017: Untangling the annual cycle of the tropical tropopause layer with
488 an idealized moist model. *Journal of Climate*, **30 (18)**, 7339–7358.

489 Laliberté, F., and P. Kushner, 2013: Isentropic constraints by midlatitude surface warming on the
490 arctic midtroposphere. *Geophysical Research Letters*, **40 (3)**, 606–611.

491 Liu, Q., 2020: Radiative kernels for Isca v1.0. Zenodo, doi:10.5281/zenodo.4282681.

492 Loeb, N. G., and Coauthors, 2018: Clouds and the earth’s radiant energy system (CERES) en-
493 ergy balanced and filled (EBAF) top-of-atmosphere (TOA) edition-4.0 data product. *Journal of*
494 *Climate*, **31 (2)**, 895–918.

495 Lu, J., and M. Cai, 2009: A new framework for isolating individual feedback processes in coupled
496 general circulation climate models. Part I: Formulation. *Clim. Dyn.*, **32**, 873–885.

497 Manabe, S., R. Stouffer, M. Spelman, and K. Bryan, 1991: Transient responses of a coupled
498 ocean–atmosphere model to gradual changes of atmospheric CO₂. Part 1. annual mean response.
499 *J. Climate*, **4 (8)**, 785–818.

500 Manabe, S., and R. J. Stouffer, 1980: Sensitivity of a global climate model to an increase of CO₂
501 concentration in the atmosphere. *Journal of Geophysical Research: Oceans*, **85 (C10)**, 5529–
502 5554.

503 Manabe, S., and R. F. Strickler, 1964: Thermal equilibrium of the atmosphere with a convective
504 adjustment. *Journal of the Atmospheric Sciences*, **21 (4)**, 361–385.

505 Manabe, S., and R. T. Wetherald, 1967: Thermal equilibrium of the atmosphere with a given
506 distribution of relative humidity. *Journal of the Atmospheric Sciences*, **24 (3)**, 241–259.

507 Merlis, T. M., T. Schneider, S. Bordoni, and I. Eisenman, 2013: Hadley circulation response to
508 orbital precession. part I: Aquaplanets. *Journal of Climate*, **26 (3)**, 740–753.

509 Mlawer, E. J., S. J. Taubman, P. D. Brown, M. J. Iacono, and S. A. Clough, 1997: Radiative trans-
510 fer for inhomogeneous atmospheres: RRTM, a validated correlated-k model for the longwave.
511 *Journal of Geophysical Research: Atmospheres*, **102 (D14)**, 16 663–16 682.

512 Payne, A. E., M. F. Jansen, and T. W. Cronin, 2015: Conceptual model analysis of the influence
513 of temperature feedbacks on polar amplification. *Geophys. Res. Lett.*, 9561–9570.

514 Pithan, F., and T. Mauritsen, 2014: Arctic amplification dominated by temperature feedbacks in
515 contemporary climate models. *Nat. Geosci.*, **7**, 181–184.

516 Roe, G. H., N. Feldl, K. C. Armour, Y.-T. Hwang, and D. M. Frierson, 2015: The remote impacts
517 of climate feedbacks on regional climate predictability. *Nature Geoscience*, **8 (2)**, 135.

518 Rose, B. E., 2018: Climlab: A python toolkit for interactive, process oriented climate modeling.
519 *J. Open Source Software*, **3 (24)**, 659.

520 Rugenstein, M., and Coauthors, 2019: LongRunMIP–motivation and design for a large collection
521 of millennial-length AO-GCM simulations. *Bulletin of the American Meteorological Society*,
522 **100 (2019)**.

523 Russotto, R. D., and M. Biasutti, 2020: Polar amplification as an inherent response of a circu-
524 lating atmosphere: results from the tracmip aquaplanets. *Geophysical Research Letters*, **47 (6)**,
525 e2019GL086 771.

526 Screen, J. A., C. Deser, and I. Simmonds, 2012: Local and remote controls on observed arctic
527 warming. *Geophysical Research Letters*, **39 (10)**.

528 Shaw, T. A., and Z. Tan, 2018: Testing latitudinally dependent explanations of the circulation
529 response to increased co2 using aquaplanet models. *Geophysical Research Letters*, **45 (18)**,
530 9861–9869.

- 531 Stocker, T. F., and Coauthors, Eds., 2013: *Climate Change 2013: The Physical Science Basis*.
532 Cambridge University Press, Cambridge and New York.
- 533 Stuecker, M. F., and Coauthors, 2018: Polar amplification dominated by local forcing and feed-
534 backs. *Nature Climate Change*, **8 (12)**, 1076.
- 535 Taylor, P. C., M. Cai, A. Hu, J. Meehl, W. Washington, and G. J. Zhang, 2013: A decomposition
536 of feedback contributions to polar warming amplification. *J. Climate*, **26**, 7023–7043.
- 537 Vallis, G. K., and Coauthors, 2018: Isca, v1. 0: A framework for the global modelling of the
538 atmospheres of Earth and other planets at varying levels of complexity. *Geoscientific Model*
539 *Development*.
- 540 Wang, Y., and Y. Huang, 2020: Understanding the atmospheric temperature adjustment to co2
541 perturbation at the process level. *Journal of Climate*, **33 (3)**, 787–803.

542 **LIST OF TABLES**

543 **Table 1.** Surface temperature change attribution based on the single column model de-
544 composition for the three perturbation experiments. ‘CO₂’ and ‘Water Vapor’
545 denote the radiative effect of their increase on surface temperature, whereas
546 ‘ET’ denotes the effect of the change in energy transport on surface tempera-
547 ture and is decomposed into its dry and moist components in the pole. ‘Q_s’
548 denotes the effect of the surface heat source on the surface temperature change.
549 ‘Diffusion’ denotes the effect of the change in diffusive temperature tendency
550 on surface temperature change. 28

551 **Table 2.** Surface temperature change attribution based on the single column model de-
552 composition for the three perturbation experiments. The tropical surface tem-
553 perature change attributions are sufficiently similar to be in a single column.
554 The three successive values separated by a comma refer to the the 4xCO₂,
555 Q_s = 12W m⁻², and Q_s = 24W m⁻² experiments respectively. Discrepancies
556 between the total and the sum of local and remote totals occur as the total is the
557 surface temperature change from the experiment with all perturbations. 29

Forcing (W m^{-2}) / Feedback ($\text{W m}^{-2} \text{K}^{-1}$)	4xCO ₂	4xCO ₂ + 12 W m^{-2}	4xCO ₂ + 24 W m^{-2}
Tropics			
CO ₂	1.9	1.9	1.9
Water Vapor	2.9	3.0	3.1
ET	-0.8	-0.6	-0.6
Diffusion	-0.43	-0.5	-0.5
Tropics total	3.5	3.8	3.8
Pole			
CO ₂	3.3	3.3	3.3
Water Vapor	4.5	5.0	5.8
ET (dry)	0.1	-1.8	-3.8
ET (moist)	1.4	1.9	2.6
Diffusion	-0.3	0.9	2.0
Q_s	0	4.3	7.2
Pole total	9.0	13.8	17.6

558 TABLE 1. Surface temperature change attribution based on the single column model decomposition for the
559 three perturbation experiments. ‘CO₂’ and ‘Water Vapor’ denote the radiative effect of their increase on surface
560 temperature, whereas ‘ET’ denotes the effect of the change in energy transport on surface temperature and is
561 decomposed into its dry and moist components in the pole. ‘ Q_s ’ denotes the effect of the surface heat source on
562 the surface temperature change. ‘Diffusion’ denotes the effect of the change in diffusive temperature tendency
563 on surface temperature change.

Forcing / feedback	Tropics	Pole (4xCO ₂)	Pole (4xCO ₂ +12)	Pole (4xCO ₂ +24)
CO ₂	1.9	3.3	3.3	3.3
q (local)	10.3	1.1	2.8	4.2
Q_s	0	0	4.3	7.2
Diffusion	-0.4	-0.3	0.9	2.0
Local total	11.8	4.0	11.2	16.6
q (remote)	-7.4,-7.3,-7.3	3.4	2.2	1.6
ET	-0.8,-0.6,-0.6	1.5	0.1	-1.2
Remote total	-8.2,-7.9,-7.9	4.8	2.3	0.5
Total	3.5,3.8,3.8	9.0	13.8	17.6

564 TABLE 2. Surface temperature change attribution based on the single column model decomposition for the
565 three perturbation experiments. The tropical surface temperature change attributions are sufficiently similar to
566 be in a single column. The three successive values separated by a comma refer to the the 4xCO₂, $Q_s = 12\text{W m}^{-2}$,
567 and $Q_s = 24\text{W m}^{-2}$ experiments respectively. Discrepancies between the total and the sum of local and remote
568 totals occur as the total is the surface temperature change from the experiment with all perturbations.

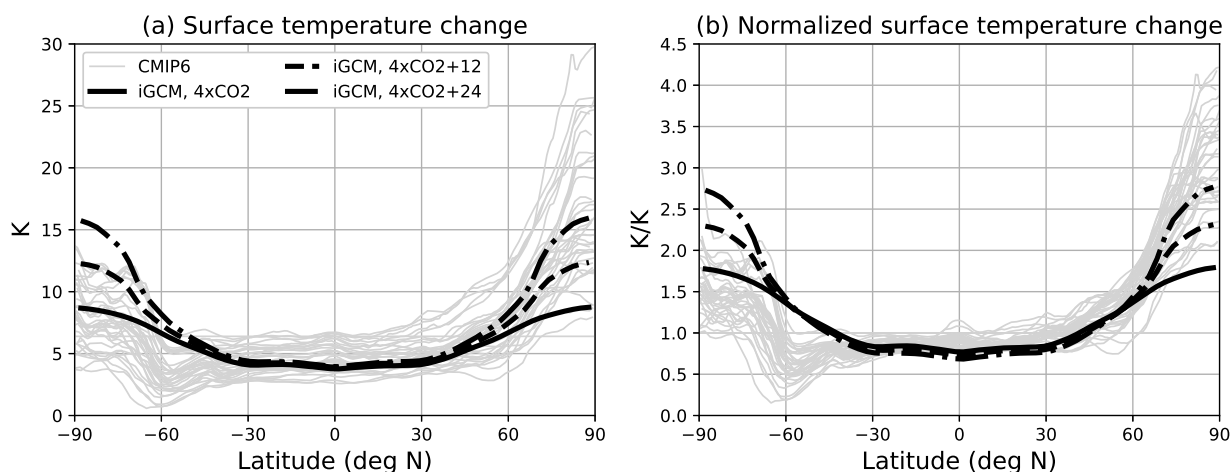
569 **LIST OF FIGURES**

570 **Fig. 1.** (a) Surface temperature difference between the control experiment (300ppm CO₂ concen-
571 tration) and increased CO₂ experiment (1200ppm) (black) and increased CO₂ experiment
572 (1200ppm) with a 12 W m⁻² (black dashed) and 24 W m⁻² (black dash-dot) surface heat
573 source poleward of 80° using an idealized moist atmospheric GCM with no clouds or
574 sea ice. These are compared to abrupt 4xCO₂ surface temperature changes in simula-
575 tions with the following models from the Coupled Model Intercomparison Project Phase 6
576 (CMIP6): ACCESS-CM2, ACCESS-ESM1-5, AWI-CM-1-1-MR, BCC-CSM2-MR, BCC-
577 ESM1, CAMS-CSM1-0, CESM2, CESM2-FV2, CESM2-WACCM, CESM2-WACCM-
578 FV2, CIESM, CMCC-CM2-SR5, CanESM5, EC-Earth3-Veg, FGOALS-f3-L, FGOALS-
579 g3, GFDL-CM4, GFDL-ESM4, GISS-E2-1-G, GISS-E2-1-H, GISS-E2-2-G, INM-CM4-
580 8, INM-CM5-0, IPSL-CM6A-LR, KACE-1-0-G, MCM-UA-1-0, MIROC6, MPI-ESM-
581 1-2-HAM, MPI-ESM1-2-HR, MPI-ESM1-2-LR, MRI-ESM2-0, NESM3, NorESM2-LM,
582 NorESM2-MM, SAM0-UNICON, TaiESM1. (b) Same as (a), but the temperature changes
583 are normalized by global-mean surface temperature change. 31

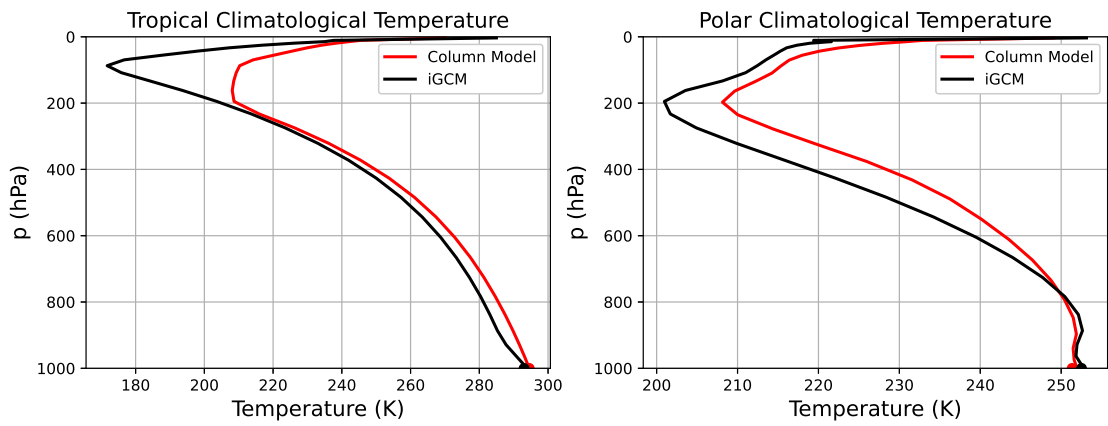
584 **Fig. 2.** Comparison between the single column model (red) and idealized GCM (black) for the (a)
585 tropical ($|\text{lat}| < 10^\circ$) climatological temperature and (b) the polar ($\text{lat} > 80^\circ$ North) climato-
586 logical temperature. 32

587 **Fig. 3.** Tropical (a) and polar (b,c,d) temperature change for the idealized GCM (grey) and three
588 perturbation experiments using the single column model: 4xCO₂ (a,b), 4xCO₂ with 12
589 W m⁻² surface heat source poleward of 80° (a,c), and 4xCO₂ with 24 W m⁻² surface heat
590 source poleward of 80° (a,d). The SCM experiments with all changes (black) are exactly the
591 same as the sum of individual changes and fit the idealized GCM (grey) well. The individ-
592 ual forcing and feedback contributions are calculated by individually perturbing them in the
593 single column model (colors). They include the CO₂ increase (red), the change in vertical
594 diffusion (magenta), the water vapor feedback (blue), the ‘local’ water vapor feedback (blue
595 dashed, see section 6), the energy transport (green in tropics, separated into dry (orange)
596 and moist (cyan) in high latitudes), and the surface heat source (yellow). The tropical tem-
597 perature changes of the three experiments (a) are similar enough to be plotted together (12
598 W m⁻² in dashed lines and 24 W m⁻² in dash-dotted lines). Surface temperature change
599 attributions are summarized in table 1. 33

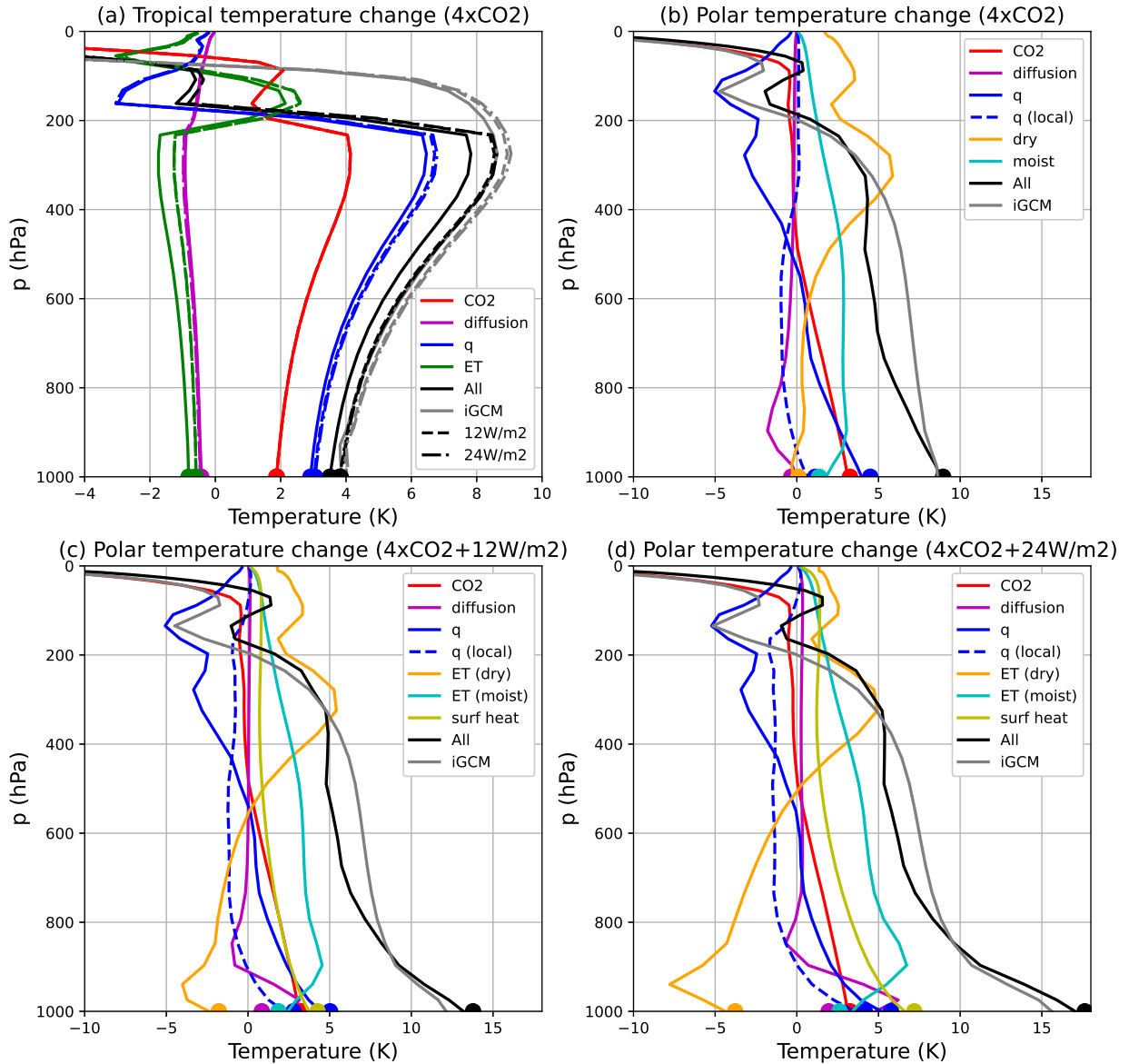
600 **Fig. 4.** Surface temperature change attributions for the 4xCO₂ (a) and 4xCO₂ with $Q_s = 12\text{W m}^{-2}$
601 (b) and $Q_s = 24\text{W m}^{-2}$ (c) using the TOA energy budget method (crosses) and the SCM
602 method presented in this paper (dots). Presented are the surface temperature change attrib-
603 utions to the increase in CO₂ (red), water vapor (blue), energy transport (green), surface heat
604 source (yellow) for both methods. The Planck (magenta) and lapse rate (cyan) feedback con-
605 tributions are also shown for the TOA energy budget method. The residual term (black) is
606 calculated as the difference between the sum of each term of the TOA energy budget method
607 and the actual surface temperature change. When the point is above (below) the one-to-one
608 line, the forcing or feedback contributes to polar (tropical) amplification. 34



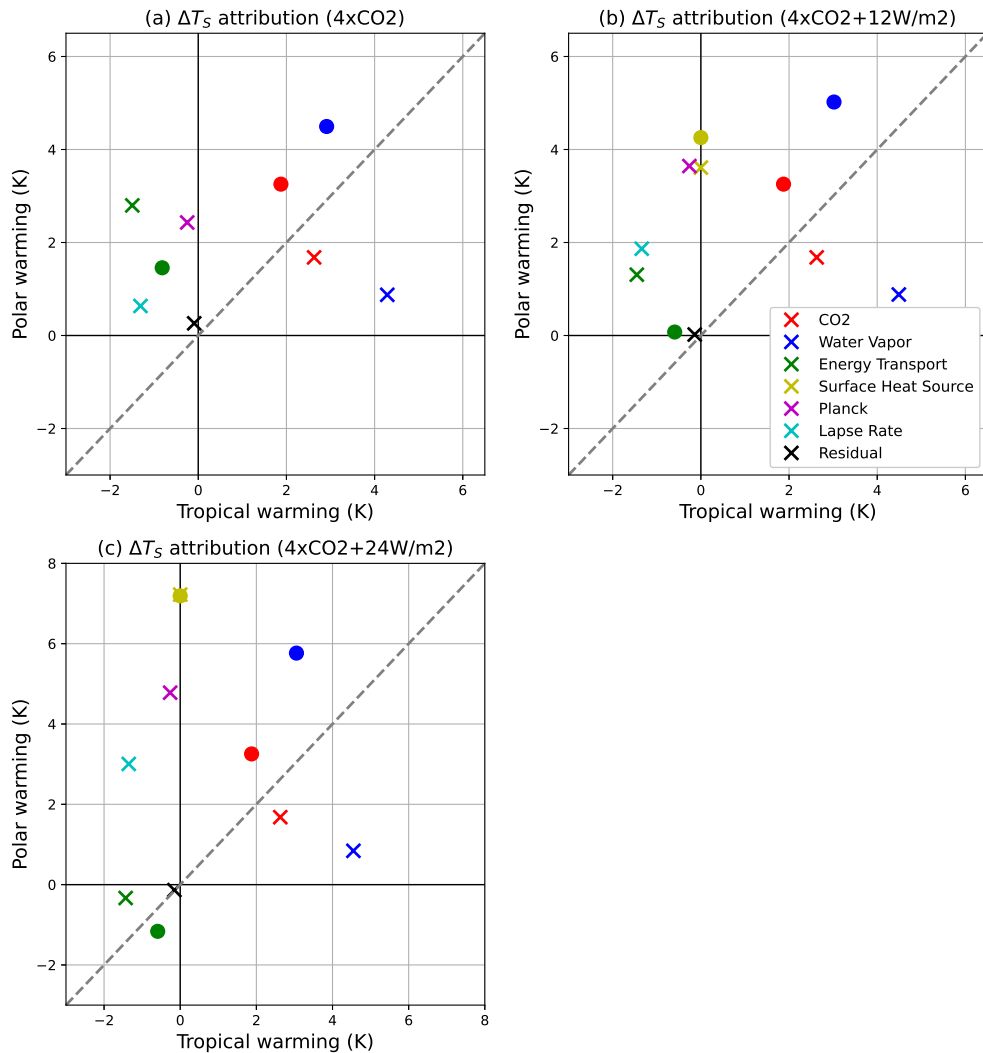
609 FIG. 1. (a) Surface temperature difference between the control experiment (300ppm CO₂ concentra-
 610 tion) and increased CO₂ experiment (1200ppm) (black) and increased CO₂ experiment (1200ppm) with a
 611 12 W m⁻² (black dashed) and 24 W m⁻² (black dash-dot) surface heat source poleward of 80° using an
 612 idealized moist atmospheric GCM with no clouds or sea ice. These are compared to abrupt 4xCO₂ sur-
 613 face temperature changes in simulations with the following models from the Coupled Model Intercompari-
 614 son Project Phase 6 (CMIP6): ACCESS-CM2, ACCESS-ESM1-5, AWI-CM-1-1-MR, BCC-CSM2-MR, BCC-
 615 ESM1, CAMS-CSM1-0, CESM2, CESM2-FV2, CESM2-WACCM, CESM2-WACCM-FV2, CIESM, CMCC-
 616 CM2-SR5, CanESM5, EC-Earth3-Veg, FGOALS-f3-L, FGOALS-g3, GFDL-CM4, GFDL-ESM4, GISS-E2-1-
 617 G, GISS-E2-1-H, GISS-E2-2-G, INM-CM4-8, INM-CM5-0, IPSL-CM6A-LR, KACE-1-0-G, MCM-UA-1-0,
 618 MIROC6, MPI-ESM-1-2-HAM, MPI-ESM1-2-HR, MPI-ESM1-2-LR, MRI-ESM2-0, NESM3, NorESM2-LM,
 619 NorESM2-MM, SAM0-UNICON, TaiESM1. (b) Same as (a), but the temperature changes are normalized by
 620 global-mean surface temperature change.



621 FIG. 2. Comparison between the single column model (red) and idealized GCM (black) for the (a) tropical
 622 ($|\text{lat}| < 10^\circ$) climatological temperature and (b) the polar ($\text{lat} > 80^\circ$ North) climatological temperature.



623 FIG. 3. Tropical (a) and polar (b,c,d) temperature change for the idealized GCM (grey) and three perturbation
 624 experiments using the single column model: 4xCO₂ (a,b), 4xCO₂ with 12 W m⁻² surface heat source poleward
 625 of 80° (a,c), and 4xCO₂ with 24 W m⁻² surface heat source poleward of 80° (a,d). The SCM experiments with
 626 all changes (black) are exactly the same as the sum of individual changes and fit the idealized GCM (grey) well.
 627 The individual forcing and feedback contributions are calculated by individually perturbing them in the single
 628 column model (colors). They include the CO₂ increase (red), the change in vertical diffusion (magenta), the
 629 water vapor feedback (blue), the ‘local’ water vapor feedback (blue dashed, see section 6), the energy transport
 630 (green in tropics, separated into dry (orange) and moist (cyan) in high latitudes), and the surface heat source
 631 (yellow). The tropical temperature changes of the three experiments (a) are similar enough to be plotted together
 632 (12 W m⁻² in dashed lines and 24 W m⁻² in dash-dotted lines). Surface temperature change attributions are
 633 summarized in table 1.



634 FIG. 4. Surface temperature change attributions for the 4xCO₂ (a) and 4xCO₂ with $Q_s = 12\text{W m}^{-2}$ (b) and
 635 $Q_s = 24\text{W m}^{-2}$ (c) using the TOA energy budget method (crosses) and the SCM method presented in this paper
 636 (dots). Presented are the surface temperature change attributions to the increase in CO₂ (red), water vapor (blue),
 637 energy transport (green), surface heat source (yellow) for both methods. The Planck (magenta) and lapse rate
 638 (cyan) feedback contributions are also shown for the TOA energy budget method. The residual term (black)
 639 is calculated as the difference between the sum of each term of the TOA energy budget method and the actual
 640 surface temperature change. When the point is above (below) the one-to-one line, the forcing or feedback
 641 contributes to polar (tropical) amplification.